STATION2RADAR: QUERY-CONDITIONED GAUSSIAN SPLATTING FOR PRECIPITATION FIELD

Anonymous authors
Paper under double-blind review

ABSTRACT

Precipitation forecasting relies on heterogeneous data. Weather radar is accurate, but coverage is geographically limited and costly to maintain. Weather stations provide accurate but sparse point measurements, while satellites offer dense, high-resolution coverage without direct rainfall retrieval. To overcome these limitations, we propose Query-Conditioned Gaussian Splatting (QCGS), the first framework to fuse automatic weather station (AWS) observations with satellite imagery for generating precipitation fields. Unlike conventional 2D Gaussian splatting, which renders the entire image plane, QCGS selectively renders only queried precipitation regions, avoiding unnecessary computation in non-precipitating areas while preserving sharp precipitation structures. The framework combines a radar point proposal network that identifies rainfall-support locations with an implicit neural representation (INR) network that predicts Gaussian parameters for each point. QCGS enables efficient, resolution-flexible precipitation field generation in real time. Through extensive evaluation with benchmark precipitation products, QCGS demonstrates over 50% improvement in RMSE compared to conventional gridded precipitation products, and consistently maintains high performance across multiple spatiotemporal scales.

1 INTRODUCTION

Recent data-driven models, including transformer-(Bi et al. (2023); Lam et al. (2023); Pathak et al. (2022); Nguyen et al. (2023); Chen et al. (2023b;a) and diffusion-(Price et al. (2025)) based forecasters trained on ERA5, now rival or surpass traditional numerical weather prediction models (NWP) at medium ranges.

Yet precipitation remains particularly challenging. (Bonavita, 2024; Liu et al., 2024; An et al., 2025) Both NWP and current global models run at coarse resolutions of tens of kilometers (e.g., ERA5), while the precipitation features most relevant for local impacts emerge at the sub-grid scale, intermittently and locally.[1] This scale mismatch complicates observation and limits the usefulness of forecasts for downstream decisions. Historically, short-range precipitation prediction relied on radar echo extrapolation at its native resolution, since NWP could not resolve small-scale convection. Operational systems therefore propagate reflectivity fields with optical-flow methods such as Lucas–Kanade (Pulkkinen et al., 2019), with skill fundamentally limited by radar fidelity. Deep learning reinforced this paradigm: radar-centric benchmarks (Veillette et al., 2020) enabled models from ConvLSTM (Shi et al., 2015) to diffusion-based nowcasting models (Gao et al., 2023; Yu et al., 2024a; Gong et al., 2024a;b) to achieve strong short-lead performance. However, precipitation forecasting is far from solved. Most pipelines assume radar as the primary input, but radar networks are costly and geographically limited, making these approaches feasible mainly in regions like Europe and the United States. Moreover, radar resolution is effectively fixed, restricting representation of processes below that scale.

These limitations motivate approaches that move beyond radar-only inputs. Conventional attempts to construct precipitation fields without radar have relied on statistical interpolation from gauges. Methods such as Barnes interpolation, kriging, or optimal interpolation (Alaka & Elvander, 1972;

[1] Rainfall often forms in localized, rapidly evolving structures smaller than the pixels of global models, leaving these subgrid-scale processes unresolved in numerical weather prediction models.

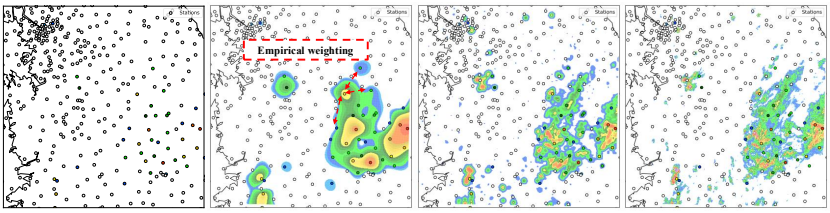

(a) Weather Station (b) Multiquadric Interpolation (c) QCGS (Ours) (d) Radar (GT)

Figure 1: Constructing precipitation fields from sparse AWS observations. (b) Classical Gaussian interpolation oversmooths and blurs rainfall boundaries. (c) QCGS leverages satellite context and gauge anchors to place Gaussians selectively, producing resolution-flexible and structurally consistent fields. (d) Ground-truth radar at 2 km for reference.

Biau et al., 1999; Barnes, 1964) represent observations by assigning Gaussian weights across a grid. While effective in principle, these interpolation methods tend to blur sharp precipitation boundaries and are highly sensitive to station density and empirically chosen kernel parameters.

Recently, satellite-only approaches such as Sat2Radar (Veillette et al., 2020; Park et al., 2025) have been proposed to approximate precipitation fields directly from spaceborne imagery. However, satellite estimates carry substantial bias and uncertainty, often provide outputs only at fixed resolution, and cannot directly leverage the physical accuracy of gauges. In parallel, several fusion-based approaches have been explored, correcting satellite products or radar imagery with gauge observations (Ruan et al., 2025; Benoit, 2021; Curcio et al., 2025). These methods improve gridded precipitation estimates by bringing them closer to ground values, but they operate strictly on fixed-resolution grids and do not cover continuous, resolution-free field reconstructions. Moreover, approaches such as (Benoit, 2021) require radar reflectivity as input, whereas our goal is explicitly radar-free precipitation generation.

In summary, radar-based methods have inherently limited spatial coverage and fixed resolution, making them unable to resolve the fine-scale rainfall features that are of operational importance.

In this work, we propose to combine satellite imagery with automatic weather station (AWS) measurements to generate precipitation fields without requiring radar. Our key insight is that the Gaussian weighting long used in objective analysis is, from a representational perspective, equivalent to Gaussian Splatting (GS) (Kerbl et al., 2023). Traditional interpolation computes a weighted sum of point observations using Gaussian kernels; GS generalizes this idea by modeling each observation as a Gaussian "blob" with learnable parameters, enabling resolution-agnostic rendering and selective concentration of computation.

Formally, Gaussian-weighted interpolation at query location $\mathbf{x}$ is

$$f_{\mathrm{GW}}(\mathbf{x}) = \frac{\sum_{i=1}^{N} K_\sigma(\mathbf{x} - \mu_i)\, y_i}{\sum_{j=1}^{N} K_\sigma(\mathbf{x} - \mu_j)}, \tag{1}$$

where y_i is the observation at station μ_i and K_σ is a Gaussian kernel. Gaussian Splatting (GS) instead defines

$$f_{\mathrm{GS}}(\mathbf{x}) = \sum_{i=1}^{N} a_i\, K_{\Sigma_i}(\mathbf{x} - \mu_i), \tag{2}$$

with learnable amplitude a_i and covariance Σ_i. Classical Gaussian weighting is recovered as a special case of GS with fixed isotropic kernels, while GS further allows anisotropy, adaptive amplitudes, and resolution-free rendering, which are key advantages for representing sharp and localized precipitation fields.

We introduce **Query-Conditioned Gaussian Splatting (QCGS)** for precipitation field generation. QCGS takes satellite imagery and automatic weather station (AWS) observations as inputs and outputs a continuous precipitation field on an arbitrary scale, without requiring radar. Unlike standard GS, which directly fits Gaussian primitives to ground-truth fields, QCGS conditions Gaussian parameters on satellite–AWS context, enabling generalization across regions and seasons.

QCGS consists of three components: (1) *Selective rendering*, which evaluates only precipitation-support regions, suppressing non-rain areas and improving efficiency. (2) *AWS–satellite fusion*, where dense satellite features provide spatial coverage and sparse AWS gauges act as accurate anchors, together proposing candidate Gaussian locations. (3) *INR-based parameterization*, in which an implicit neural network maps local satellite features and query locations to Gaussian parameters (amplitude and covariance), allowing adaptive, anisotropic blob shapes and resolution-free rendering.

Through this design, QCGS moves beyond traditional empirical weighting (as illustrated in Fig. 1) and produces high-resolution precipitation fields that preserve sharp structures, remain computationally efficient, and generalize effectively.

2 Related Work

We discuss three relevant areas: Gaussian Splatting for efficient field generation, Implicit Neural Representations (INR) for coordinate-conditioned modeling, and data-driven methods in meteorology.

2.1 Gaussian Splatting

3D Gaussian Splatting (3DGS) (Kerbl et al., 2023) accelerates NeRF (Mildenhall et al., 2021) by representing scenes with Gaussian kernels and avoiding redundant rendering, enabling real-time performance (Wu et al., 2024; Huang et al., 2024; Yu et al., 2024b; Guédon & Lepetit, 2024; Yang et al., 2024). Recent work has extended this idea to 2D images for compression and super-resolution, such as GaussianImage (Zhang et al., 2024), Image-GS (Zhang et al., 2025), and LIG (Zhu et al., 2025), which allocate Gaussians adaptively based on gradients or frequency content. Follow-ups like GaussianSR (Hu et al., 2025), ContinuousSR (Peng et al., 2025), and GSASR (Chen et al., 2025) introduced kernel banks and feed-forward prediction for scalability and generalization. While effective, these methods remain image-specific, motivating our adaptation to precipitation fields.

2.2 Implicit Neural Representations

INR (Sitzmann et al., 2020) encodes signals as continuous coordinate-to-value mappings, widely applied to 3D scene reconstruction (Mildenhall et al., 2021; Barron et al., 2021; Martin-Brualla et al., 2021; Barron et al., 2022; Müller et al., 2022), image compression, and arbitrary-scale super-resolution (Chen et al., 2021; Yang et al., 2021; Cao et al., 2023; Lee & Jin, 2022). Its strength lies in resolution-free modeling, but INRs must query all coordinates and lack explicit spatial structure, limiting efficiency. Nonetheless, their representational flexibility motivates our query-conditioned adaptation for precipitation fields.

2.3 Applications of Deep Learning in Meteorology

Deep learning has transformed meteorology, especially in precipitation nowcasting and weather prediction. ConvLSTM (Shi et al., 2015) pioneered spatiotemporal forecasting, followed by GAN-based (Ravuri et al., 2021) and transformer-based (Bi et al., 2023) approaches that rival or surpass NWP models. More recent methods span precipitation forecasting (Gao et al., 2022b; Veillette et al., 2020; Gong et al., 2024a; Yu et al., 2024a; Yoon et al., 2023; Gao et al., 2023) and global atmospheric variable prediction (Bi et al., 2023; Lam et al., 2023; Kochkov et al., 2024; Chen et al., 2023b; Xu et al., 2024; Xiao et al., 2023). Despite progress, most rely on radar or reanalysis data (e.g., ERA5). Recent data assimilation methods (Xiao et al., 2023) attempt to reduce this dependency, but to our knowledge, our work is the first to directly generate precipitation initial conditions from satellite and station data.

3 Preliminaries

We summarize the key notions from the perspective of *2D image rendering*.

Implicit Neural Representations (INR). An INR models an image as a continuous function

$$f_\theta : \mathbb{R}^2 \to \mathbb{R}^C,$$

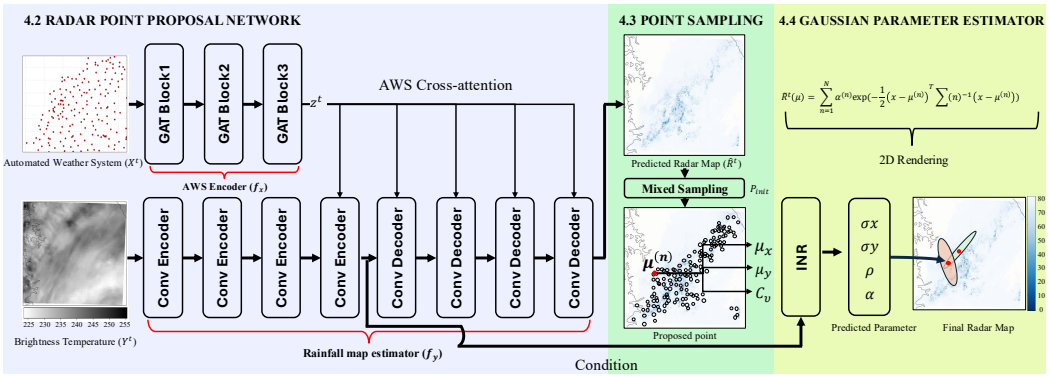

Figure 2: Overview of the proposed QCGS pipeline. AWS observations and satellite BT imagery are fused to produce a coarse surrogate field and candidate rainfall-support points. A rainfall-aware sampling strategy and an INR-based Gaussian estimator then predict splatting parameters, yielding resolution-flexible precipitation fields via selective Gaussian rendering.

that maps *spatial coordinates* $\mathbf{x} \in \mathbb{R}^2$ to values. Rendering an $H \times W$ image requires evaluating f_θ at all pixel centers $\mathbf{x} \in \Omega$, which scales as $\mathcal{O}(HW)$. INRs are resolution-free and differentiable w.r.t. coordinates, but dense querying makes high-resolution synthesis slow.

Gaussian Splatting. 3D Gaussian Splatting (3DGS) represents a scene as a set of anisotropic 3D Gaussian primitives. Each primitive has a center $\mu_k \in \mathbb{R}^3$, covariance $\Sigma_k \in \mathbb{S}^3_{++}$, opacity α_k, and color c_k. Rendering proceeds by projecting the Gaussians to the image plane, linearizing the covariance with the Jacobian of the projection, and compositing front-to-back with depth ordering:

$$I(u) = \sum_{k=1}^{K} T_k(u)\, \alpha_k\, G_k(u)\, c_k,$$

where $T_k(u)$ is the accumulated transmittance and $G_k(u)$ the screen-space Gaussian footprint.

In contrast, **2D Gaussian Splatting (2DGS)** removes geometry-specific elements and operates directly on the image plane. No 3D positions, projections, or depth ordering are required. Each primitive is simply a 2D Gaussian with center

$$\boldsymbol{\mu}_i \in \mathbb{R}^2, \qquad \Sigma_i \in \mathbb{S}^2_{++}, \qquad \alpha_i \in \mathbb{R}.$$

The rendered value at a pixel location $\mathbf{x} \in \Omega$ is

$$I(\mathbf{x}) = \sum_{i=1}^{K} \alpha_i \exp\Big(-\tfrac{1}{2}(\mathbf{x} - \boldsymbol{\mu}_i)^\top \Sigma_i^{-1} (\mathbf{x} - \boldsymbol{\mu}_i) \Big).$$

Thus 2DGS retains the resolution-free rendering benefits of 3DGS while being simpler and computationally cheaper, making it well suited for representing sharp, localized precipitation fields.

4 METHOD

As illustrated in Fig. 2, QCGS follows a three-stage pipeline that fuses AWS gauge observations with satellite imagery to generate precipitation fields. Importantly, the radar point proposal network and the Gaussian rendering module are trained separately.

We first train the radar point proposal network to produce reliable rainfall-support locations, and then train the Gaussian rendering stage on top of these fixed proposals. Thus, QCGS operates as a two-stage model in terms of training, even though the full pipeline consists of three conceptual components.

4.1 TASK DEFINITION

We aim to estimate a high-resolution precipitation field $R^t(\mathbf{x})$ using two inputs at time t: a satellite image $Y^t \in \mathbb{R}^{H\times W}$ and sparse AWS measurements $X^t = \{x_i^t \mid i \in \mathcal{I}\}$ located at irregular coordinates $\{\mu_i\}$.

Formally, the goal is to learn a mapping

$$\mathcal{F}_\Theta : \ (Y^t, X^t) \ \longmapsto \ R^t(\mathbf{x}), \qquad \mathbf{x} \in \Omega,$$

where Ω denotes a continuous 2D spatial domain. Unlike standard Sat→Radar image-to-image translation (Park et al., 2025), our input consists of *both* a dense image and an irregular point set, and the output must be defined on *arbitrary* query locations rather than a fixed grid.

Because the satellite image is coarse (2 km resolution) and the output precipitation field may be queried at much finer scales (e.g., 0.5 km or continuous coordinates), the task also exhibits a super-resolution nature:

$$R^t : \Omega_{\text{coarse}} \ \rightarrow \ \Omega_{\text{fine}}, \qquad |\Omega_{\text{fine}}| \gg |\Omega_{\text{coarse}}|.$$

The model parameters are estimated by minimizing reconstruction loss against radar observations during training:

$$\Theta^* = \arg\min_{\Theta} \ \mathcal{L}\big(R^t, \ \mathcal{F}_\Theta(Y^t, X^t)\big),$$

In summary, the task is a hybrid problem combining *image + point fusion*, *continuous field reconstruction*, and *resolution-free rendering*.

4.2 RADAR POINT PROPOSAL NETWORK

Automatic weather station (AWS) observations provide direct gauge measurements of rainfall. Although they offer ground truth rainfall values, the data are sparse and often contain missing values or outliers. In contrast, satellite-based brightness temperature (BT) imagery $Y^t \in \mathbb{R}^{H\times W}$ provides dense spatial coverage and is generally reliable, but it only correlates indirectly with precipitation. We combine these two complementary sources to compensate for their respective limitations.

At each time step $t \in \mathcal{T}$, the set of AWS observations is defined as

$$X^t = \{x_i^t \mid i \in \mathcal{I}\}, \quad \mathcal{I} = \{1, \ldots, n\},$$

where x_i^t denotes the rainfall measured at station i and $n = |\mathcal{I}|$ is the number of stations. Since X^t may include missing values or anomalies, we employ a graph attention network (Velickovic et al., 2017) $f_x(\cdot;\theta_x)$ to extract a robust representation:

$$z^t = f_x(X^t).$$

The satellite BT image Y^t is processed by an encoder–decoder network $f_y(\cdot;\theta_y)$ to produce a dense rainfall prediction:

$$\hat{R}^t = f_y(Y^t, z^t),$$

where the AWS representation z^t is fused with the decoder via cross-attention.

During training, the model parameters are optimized by minimizing the mean squared error (MSE) between the predicted rainfall $\hat{R}^t$ and the radar-derived ground truth R^t:

$$\mathcal{L}_{\text{MSE}} = \frac{1}{|\mathcal{T}|} \sum_{t\in\mathcal{T}} \big\|\hat{R}^t - R^t\big\|_2^2.$$

4.3 RAINFALL-AWARE POINT SAMPLING

In precipitation forecasting, light rain rarely leads to disasters, while heavy precipitation events are much more likely to trigger hazards and accidents. Therefore, the most critical objective is to accurately predict regions of heavy precipitation. Uniformly sampling points across the entire

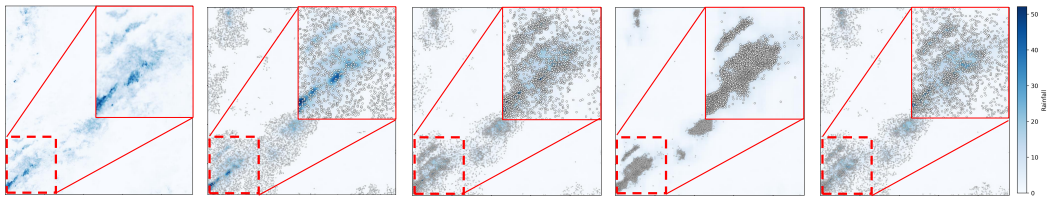

Figure 3: Visualization of different point sampling strategies for precipitation fields. (a) Ground truth radar field, (b) uniform sampling, (c) edge-based sampling, (d) heavy-rain sampling, and (e) our mixed strategy. Uniform sampling provides overall coverage but fails to capture details in heavy rainfall regions. Edge-based sampling emphasizes boundaries but overlooks texture information. Heavy-rain sampling concentrates points on strong precipitation, leaving light-rain areas underrepresented. In contrast, our mixed strategy balances these factors, yielding both accurate representation of heavy rainfall and adequate spatial coverage across the entire field.

prediction field $\hat{R}^t$ is inefficient, as it treats all regions equally regardless of their importance. To overcome this limitation, we design a sampling strategy that incorporates three factors: (1) gradients of $\hat{R}^t$ to emphasize edges, (2) uniform coverage within $\hat{R}^t$, and (3) rainfall intensity to prioritize heavy-rain regions.

We denote image-domain coordinates as $\mathbf{x} \in \Omega$, and write $\hat{R}^t(\mathbf{x})$ for its rainfall value.

Let $\hat{R}^t \in \mathbb{R}^{H \times W}$ be a coarse precipitation field at time t, and define the rain-support mask as

$$\mathcal{S}_t = \{\mathbf{x} \mid \hat{R}^t(\mathbf{x}) > \tau\},$$

with a threshold τ. We then construct a convex mixture of three normalized terms:

$$P_{\text{init}}(\mathbf{x}) = \alpha\, G_{\mathcal{S}_t}(\mathbf{x}) + \beta\, U_{\mathcal{S}_t}(\mathbf{x}) + \gamma\, H(\mathbf{x}), \qquad \alpha, \beta, \gamma \geq 0, \;\; \alpha + \beta + \gamma = 1,$$

where

$$U_{\mathcal{S}_t}(\mathbf{x}) = \frac{\mathbb{1}\{\mathbf{x} \in \mathcal{S}_t\}}{\sum_{h,w} \mathbb{1}\{(h,w) \in \mathcal{S}_t\} + \varepsilon}, \quad G_{\mathcal{S}_t}(\mathbf{x}) = \frac{\mathbb{1}\{\mathbf{x} \in \mathcal{S}_t\}\, \|\nabla \hat{R}^t(\mathbf{x})\|_2}{\sum_{h,w} \mathbb{1}\{(h,w) \in \mathcal{S}_t\}\, \|\nabla \hat{R}^t(h,w)\|_2 + \varepsilon}, \quad H(\mathbf{x}) = \frac{\exp(\hat{R}^t(\mathbf{x})/T)}{\sum_{h,w} \exp(\hat{R}^t(h,w)/T)}.$$

Here, $\nabla \hat{R}^t(\mathbf{x})$ denotes the spatial gradient of the coarse precipitation field, $T > 0$ is a temperature parameter controlling the sharpness toward heavy-rain pixels, and $\varepsilon > 0$ is a small constant (set to 10^{-8} in our experiments) introduced to ensure numerical stability when the denominator approaches zero.

4.4 INR-based Gaussian Parameter Estimator

Our objective is to generate dense, high-quality precipitation fields from satellite imagery and sparse AWS observations, even without radar ground truth. Conventional Gaussian splatting often overfits to a single image and does not generalize; we instead design an INR-based estimator that predicts Gaussian parameters only at rainfall-support queries, avoiding unnecessary computation in dry regions.

Given proposal points $\mu^{(n)} = \{(u_x^{(n)}, u_y^{(n)}, s^{(n)})\}_{n=1}^{N}$ from the Radar Point Proposal Network, the estimator is conditioned on intermediate satellite features $f_y(Y^t, z^t) \in \mathbb{R}^{H' \times W' \times D}$. Through cross-attention, we predict Gaussian parameters

$$\theta^{(n)} = \{\sigma_x^{(n)}, \sigma_y^{(n)}, \rho^{(n)}, \alpha^{(n)}\},$$

where $(\sigma_x^{(n)}, \sigma_y^{(n)}, \rho^{(n)})$ define the covariance $\Sigma^{(n)} \in \mathbb{S}_{++}^2$ and $\alpha^{(n)}$ controls the Gaussian amplitude. At AWS stations with nonzero rainfall, we directly set $\alpha^{(n)} = s^{(n)}$, anchoring the field to ground-truth observations.

Training minimizes reconstruction error against radar fields with regularization:

$$\mathcal{L} = \frac{1}{|\Omega|} \sum_{\mathbf{x} \in \Omega} (\tilde{R}^t(\mathbf{x}) - R^t(\mathbf{x}))^2 + \lambda_\sigma \sum_n (\sigma_x^{(n)} + \sigma_y^{(n)}) + \lambda_\alpha \sum_n \alpha^{(n)}.$$

The final precipitation map is rendered by differentiable 2D Gaussian splatting:

$$\tilde{R}^t(\mathbf{x}) = \sum_{n=1}^{N} \alpha^{(n)} \exp\Big(-\tfrac{1}{2}(\mathbf{x}-\mu^{(n)})^\top {\Sigma^{(n)}}^{-1} (\mathbf{x}-\mu^{(n)}) \Big),$$

with $\mu^{(n)} = (u_x^{(n)}, u_y^{(n)})$. This operator is fully differentiable, enabling end-to-end training.

5 Experiments

We evaluate QCGS on satellite and AWS gauge data from 2023, and compare against both classical gridded precipitation products (IMERG from the national aeronautics and space administration (NASA), MSWEP from University of Maryland, GSMaP from the Japan aerospace exploration agency (JAXA)) and deep learning baselines based on image-to-image translation.

5.1 Experimental Setting

Dataset. We use three data sources: (i) automatic weather station (AWS) gauges providing sparse point-wise rainfall measurements over land, (ii) GK2A geostationary satellite imagery (IR 10.5μm channel, 2 km resolution), and (iii) KMA HSP weather radar fields (0.5 km resolution). We crop the study domain to a 480×480 grid ($35.5°$–$37.8°$N, $126.4°$–$129.1°$E), where gauge density is relatively high. Models are trained on hourly data from 2019–2022 and validated on 2023. Although training is performed at 2 km resolution, we also evaluate at 0.5 km to demonstrate the ability of QCGS to render rainfall fields at arbitrary scales.

Evaluation Metrics. We evaluate QCGS using RMSE for overall error and LPIPS (Zhang et al., 2018) for perceptual similarity. For grid-point verification, we report Critical Success Index (CSI), Categorical CSI, Fraction Skill Score (FSS; Roberts & Lean (2008)) with a 5×5 window, and bias. We also compute Pearson and Spearman correlations to assess spatial patterns and extremes.

Comparison Methods. We benchmark QCGS against three categories of baselines. For classical interpolation, we use Barnes (Barnes, 1973), Multi-quadric(MQ, Nuss & Titley (1994)), and Kriging (Lucas et al., 2022) methods. For operational products, we include IMERG (Huffman et al., 2015) (NASA), a global 0.1° multi-satellite retrieval widely used in hydrology; MSWEP (Beck et al., 2019) (University of Maryland), a long-term 0.1° dataset that blends gauges, satellite, and reanalysis; and GSMaP (Mega et al., 2018) (JAXA), a near–real-time 0.1° product combining passive microwave radiometers with geostationary infrared sensors. We also compare GK2A rain rate 2-km product as regional quantitative precipitation estimation. For data-driven baselines, we compare against NPM (Park et al., 2025), the first model to demonstrate precipitation forecasting from satellite imagery alone, where we use the sat-to-radar stage for fairness; BBDM (Li et al., 2023), a diffusion-based image-to-image framework adapted for precipitation downscaling; and Pix2PixHD (Wang et al., 2018), a conditional GAN commonly applied to satellite-to-rainfall mapping, though often limited in preserving sharp convective structures.

By comparing against both operational references and learning-based models, we ensure that QCGS is evaluated against the full spectrum of established standards and state-of-the-art deep methods.

Implementation Details. We fix the number of query points to $K{=}6000$, which provides a optimal balance between fidelity and efficiency. The surrogate radar field $\hat{R}$ is produced by a ConvNeXt-based U-Net with four encoder/decoder stages and skip connections, using group normalization and GELU activations. AWS observations are embedded via a three-layer Graph Attention Network (8 heads, hidden size 128) and fused with satellite features in the decoder through cross-attention.

For point selection, we adopt a rainfall-aware strategy combining edge, intensity, and uniform terms (0.3/0.4/0.3), with non-maximum suppression to avoid redundancy. Each query is passed to a five-layer MLP INR (hidden size 128, sinusoidal encoding), which predicts Gaussian parameters $\{\sigma_x, \sigma_y, \rho, \alpha\}$. At AWS sites with nonzero rainfall, α is set directly to the observed value, anchoring the generated fields.

Table 1: Quantitative results across multiple spatiotemporal scales. Each block shows the number of evaluated cases in parentheses. QCGS is trained at 2 km and downsampled to 0.1° for comparison with global products. Best scores per block are in **bold**.

Temporal scale (cases)	Category	Method	Res.	RMSE↓	LPIPS↓	CSI↑	FSS↑	CC↑	Bias≈1
Snapshot (1154)	Data-driven	Pix2PixHD	0.5 km	2.45	0.62	0.59	0.71	0.55	0.82
	Data-driven	NPM	0.5 km	1.95	0.58	0.59	0.78	0.68	0.88
	Data-driven	BBDM	0.5 km	1.68	0.54	0.64	0.84	0.75	0.93
	Satellite Product	GK2A	2.0 km	2.89	0.40	0.20	0.37	0.12	-
	Classical Interp.	Barnes	2.0 km	2.56	0.39	0.47	0.68	0.42	0.98
	Classical Interp.	Kriging	2.0 km	2.43	0.40	0.50	0.69	0.45	1.03
	Classical Interp.	3DMQ	2.0 km	2.47	0.41	0.49	0.68	0.44	1.00
	Ours	QCGS	0.5 km	1.23	0.49	0.74	0.91	0.90	1.02
	Ours	QCGS	2.0 km	**1.00**	**0.19**	**0.76**	**0.96**	**0.93**	1.03
Hourly mean (1154)	Satellite Product	IMERG	0.1°	1.66	0.34	0.50	0.72	0.42	0.85
	Satellite Product	GSMaP	0.1°	1.95	0.38	0.43	0.64	0.39	0.78
	Ours	QCGS	0.1°	**1.33**	**0.21**	**0.66**	**0.93**	**0.74**	0.97
Daily accum. (70)	Satellite Product	IMERG	0.1°	14.08	0.33	0.85	0.92	0.72	0.95
	Satellite Product	GSMaP	0.1°	15.89	0.35	0.92	0.82	0.70	0.88
	Satellite Product	MSWEP	0.1°	12.44	0.32	**0.95**	0.91	0.78	1.07
	Ours	QCGS	0.1°	**6.68**	**0.21**	0.93	**0.99**	**0.95**	1.02

Training uses Adam (1×10^{-4} initial lr, 1×10^{-5} weight decay, cosine schedule, gradient clipping at 1.0), batch size 16, for 100 epochs. Regularization terms $\lambda_\sigma = 10^{-3}$ and $\lambda_\alpha = 10^{-4}$ prevent over-smoothing. All experiments are conducted on 8×NVIDIA H200 GPUs.

5.2 Quantitative results

Comparison with data-driven approaches. All data-driven baselines (Pix2PixHD, NPM, BBDM) were trained and evaluated directly at 0.5 km resolution for fairness. In contrast, QCGS was trained only at 2 km resolution and later rendered to 0.5 km during evaluation. Despite this apparent disadvantage, QCGS consistently achieved the best performance across all metrics, as summarized in Table 1. This robustness can be explained by two key design choices.

First, QCGS explicitly fuses AWS observations. Although gauges are sparse, their ground-level accuracy provides strong local anchors that substantially enhance field reconstruction and correct biases that purely satellite-driven models cannot address. Our ablation study (Sec. 5.4) confirms this, since removing AWS information causes a sharp decline in both pixel-wise accuracy and spatial correlation.

Second, QCGS leverages Gaussian Splatting (GS) to achieve resolution-free rendering. While existing models are tied to the resolution of their training grid (for example, 0.5 km), GS allows QCGS to generate rainfall fields at arbitrary scales while focusing computation on rainfall-support regions. This capability preserves fine-scale convective boundaries without requiring retraining, in contrast to conventional super-resolution methods that often blur or oversmooth extremes.

Taken together, AWS fusion and GS-based resolution-free rendering explain why QCGS outperforms models trained at higher resolution. Table 1 highlights this advantage clearly, showing that even with 2 km training QCGS surpasses state-of-the-art 0.5 km baselines in both accuracy and structural fidelity.

Comparison with classical interpolation. Classical interpolation methods such as Barnes, Kriging, and 3DMQ rely on fixed Gaussian kernels to spread each gauge observation across the grid. As shown in Table 1, these approaches produce smooth rainfall patterns with limited structural fidelity. Their RMSE values remain above 2.4 at 2 km resolution, and their CSI and FSS scores saturate around 0.47–0.50 and 0.68–0.69, respectively. This reflects the inherent limitation of using static, isotropic kernels that cannot adapt to precipitation geometry, resulting in blurred boundaries and underestimation.

In contrast, QCGS learns anisotropic and spatially adaptive Gaussian primitives conditioned on satellite features, enabling sharper and more meteorologically consistent rainfall structures. QCGS reduces RMSE to 1.00 at 2 km, and improves CSI from 0.50 (Kriging) to 0.76 and FSS from 0.69 to

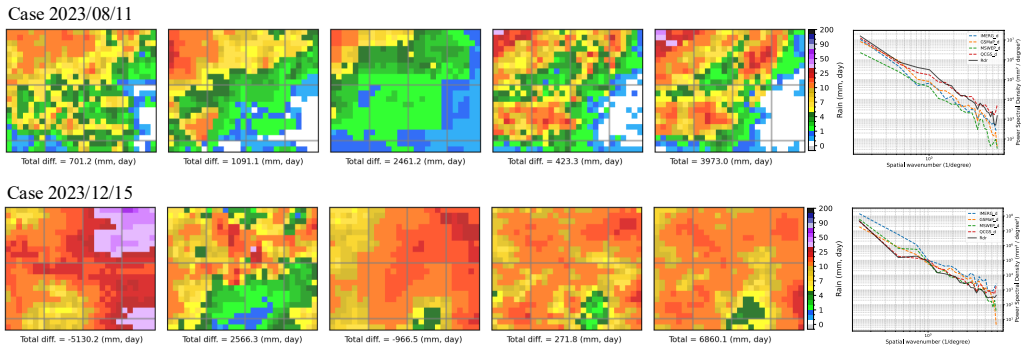

(a) IMERG (b) GSMaP (c) MSWEP (d) QCGS (e) Radar (f) PSD plot

Figure 4: Panels (a)–(e) show the comparison of daily accumulated rainfall (mm, day) between radar and four rainfall products: IMERG, GSMaP, MSWEP, and QCGS. The "total diff." panel indicates the difference between radar and each product. Panel (f) the PSD at different scales (=wavelengths), at different cases.

0.96, representing a substantial improvement across all metrics. These results demonstrate that QCGS generalizes classical Gaussian-weighted interpolation and significantly enhances its representational capacity for high-resolution precipitation field reconstruction.

Comparison with operational products. We benchmarked QCGS against operational datasets including IMERG (NASA/GSFC), GSMaP (JAXA), and MSWEP (Utrecht). These products provide global coverage, are purely satellite–driven, and apply sophisticated bias correction using rain gauges and reanalysis, which often reduces systematic errors. Nevertheless, as shown in Table 1, QCGS achieves consistently lower RMSE and higher correlation, despite being trained only with regional satellite imagery and sparse AWS measurements.

For fairness, 10-minute radar was aggregated into hourly means and daily accumulations, and all datasets were reprojected to radar coordinates using GDAL. QCGS outputs were trained at 2 km and later downsampled to 0.1° grids for comparison.

The key advantage of QCGS is that AWS fusion anchors local rainfall intensities, enabling sharper and more accurate regional fields than purely satellite products. At the same time, this also represents a limitation: whereas IMERG, GSMaP, and MSWEP remain purely satellite-based and thus globally deployable, QCGS currently depends on sparse but precise ground observations. In other words, QCGS delivers higher fidelity at regional scales, while operational products retain broader applicability.

5.3 Qualitative Results

Case study and spectral analysis. Figure 4 compares daily accumulated precipitation from radar, three operational products (IMERG, GSMaP, MSWEP), and QCGS. QCGS produces fields visually closest to radar, reducing absolute differences and preserving localized convective cells. By contrast, GSMaP systematically underestimates intensity, while IMERG and MSWEP exhibit case-dependent over- and underestimation.

The power spectral density (PSD) analysis further shows that QCGS matches radar across most scales, retaining both large-scale organization and mesoscale structure. Operational products lose variance at high wavenumbers, with MSWEP appearing oversmoothed. QCGS slightly overestimates the smallest scales, reflecting both preserved subgrid variation and minor artifacts. Overall, QCGS maintains the spectral balance of precipitation fields better than existing products.

5.4 Ablation Study

Architecture (Table 2-(a)). Starting from a U-Net (ConvNeX) trained for Sat to RDR translation, adding AWS fusion provides a clear improvement by anchoring rainfall intensities at gauge locations.

Table 2: Comprehensive ablation study on CSI. (a) Effect of architecture choices: AWS fusion and Gaussian Splatting (GS) progressively improve performance. (b) Effect of sampling strategy: combining gradient, regular, and heavy-rain sampling yields the best CSI. (c) Effect of the number of query points: performance saturates around K=6000. Best results are in **bold**.

Architecture	CSI↑
AWS (only)	0.53
U-Net (ConvNeXt)	0.62
+ AWS fusion	0.73
+ AWS fusion + GS (ours)	**0.76**

(a) Architecture.

Reg.	Grad.	Heavy	CSI↑
✓			0.68
	✓		0.71
		✓	0.70
✓	✓		0.73
	✓	✓	0.74
✓		✓	0.72
✓	✓	✓	**0.76**

(b) Sampling strategy.

K points	CSI↑
1000	0.69
3000	0.72
6000	0.76
9000	**0.77**

(c) Number of query points.

Incorporating Gaussian Splatting (GS) further improves performance by enabling resolution-free rendering of localized rainfall, achieving the highest CSI.

Sampling strategy (Table 2-(b)). Regular interval sampling alone performs the worst, while gradient- or heavy-rain–based strategies provide moderate gains. Combining all three (gradient, regular, heavy-rain) yields the best CSI (0.76), confirming the importance of jointly covering boundaries, background regions, and rainfall extremes.

Number of query points (Table 2-(c)). Increasing the number of sampled points K steadily improves CSI up to K=6000, where the score reaches 0.76. Using more points (K=9000) yields only a marginal gain (0.77) while increasing computation, so we adopt K=6000 as the default trade-off between accuracy and efficiency.

6 Conclusion

We introduced Query-Conditioned Gaussian Splatting (QCGS), a framework for generating high-quality precipitation fields from sparse and heterogeneous observations. By treating each observation as a Gaussian kernel and conditioning splatting on satellite imagery, QCGS selectively renders rainfall regions, reducing computation while preserving sharp boundaries. The integration of Implicit Neural Representations further enables resolution-free parameterization and strong generalization across regions and seasons. Extensive experiments show that QCGS mitigates representativeness errors, reconstructs rainfall even in gauge-sparse settings, and produces resolution-flexible fields that align closely with radar observations. These outputs are valuable not only for data assimilation but also as high-quality training data for data-driven forecasting, bridging the gap between point-based and gridded products. Overall, QCGS provides a scalable and physically consistent approach to multi-source precipitation integration, offering a promising pathway for enhancing both traditional NWP systems and emerging AI-based weather prediction models.

Limitations and Future Work Despite its strengths, QCGS has two main limitations. First, the method relies on automatic weather station (AWS) data to anchor rainfall intensities. In regions with insufficient gauge networks, its applicability is therefore limited. Second, our experiments were confined to the regional scale; scaling up the approach to the global domain remains an open challenge.

Looking forward, we see two promising directions. An intriguing observation is that QCGS-generated fields already align more closely with AWS measurements than raw radar reflectivity, even without any reflectivity-to-rainfall correction Fig. 6. This suggests that QCGS may offer bias-free alternatives to conventional radar products. Future work will further investigate this property, with the long-term goal of extending QCGS toward a scalable, global system that can complement or even substitute radar-based precipitation monitoring.

REFERENCES

Mikhail A Alaka and Robert C Elvander. Optimum interpolation from observations of mixed quality. *Monthly Weather Review*, 100(8):612–624, 1972.

Sojung An, Tae-Jin Oh, Eunha Sohn, and Donghyun Kim. Deep learning for precipitation nowcasting: A survey from the perspective of time series forecasting. *Expert Systems with Applications*, 268: 126301, 2025.

Stanley L Barnes. A technique for maximizing details in numerical weather map analysis. *Journal of Applied Meteorology (1962-1982)*, pp. 396–409, 1964.

Stanley L Barnes. Mesoscale objective map analysis using weighted time-series observations. 1973.

Jonathan T Barron, Ben Mildenhall, Matthew Tancik, Peter Hedman, Ricardo Martin-Brualla, and Pratul P Srinivasan. Mip-nerf: A multiscale representation for anti-aliasing neural radiance fields. In *Proceedings of the IEEE/CVF international conference on computer vision*, pp. 5855–5864, 2021.

Jonathan T Barron, Ben Mildenhall, Dor Verbin, Pratul P Srinivasan, and Peter Hedman. Mip-nerf 360: Unbounded anti-aliased neural radiance fields. In *Proceedings of the IEEE/CVF conference on computer vision and pattern recognition*, pp. 5470–5479, 2022.

Hylke E Beck, Eric F Wood, Ming Pan, Colby K Fisher, Diego G Miralles, Albert IJM Van Dijk, Tim R McVicar, and Robert F Adler. Mswep v2 global 3-hourly 0.1 precipitation: methodology and quantitative assessment. *Bulletin of the American Meteorological Society*, 100(3):473–500, 2019.

Lionel Benoit. Radar and rain gauge data fusion based on disaggregation of radar imagery. *Water Resources Research*, 57(2):e2020WR027899, 2021.

Kaifeng Bi, Lingxi Xie, Hengheng Zhang, Xin Chen, Xiaotao Gu, and Qi Tian. Accurate medium-range global weather forecasting with 3d neural networks. *Nature*, 619(7970):533–538, 2023.

Gérard Biau, Eduardo Zorita, Hans von Storch, and Hans Wackernagel. Estimation of precipitation by kriging in the eof space of thesea level pressure field. *Journal of Climate*, 12(4):1070–1085, 1999.

Massimo Bonavita. On some limitations of current machine learning weather prediction models. *Geophysical Research Letters*, 51(12):e2023GL107377, 2024.

Jiezhang Cao, Qin Wang, Yongqin Xian, Yawei Li, Bingbing Ni, Zhiming Pi, Kai Zhang, Yulun Zhang, Radu Timofte, and Luc Van Gool. Ciaosr: Continuous implicit attention-in-attention network for arbitrary-scale image super-resolution. In *Proceedings of the IEEE/CVF Conference on Computer Vision and Pattern Recognition*, pp. 1796–1807, 2023.

Du Chen, Liyi Chen, Zhengqiang Zhang, and Lei Zhang. Generalized and efficient 2d gaussian splatting for arbitrary-scale super-resolution. *arXiv preprint arXiv:2501.06838*, 2025.

Kang Chen, Tao Han, Junchao Gong, Lei Bai, Fenghua Ling, Jing-Jia Luo, Xi Chen, Leiming Ma, Tianning Zhang, Rui Su, et al. Fengwu: Pushing the skillful global medium-range weather forecast beyond 10 days lead. *arXiv preprint arXiv:2304.02948*, 2023a.

Lei Chen, Xiaohui Zhong, Feng Zhang, Yuan Cheng, Yinghui Xu, Yuan Qi, and Hao Li. Fuxi: a cascade machine learning forecasting system for 15-day global weather forecast. *npj climate and atmospheric science*, 6(1):190, 2023b.

Yinbo Chen, Sifei Liu, and Xiaolong Wang. Learning continuous image representation with local implicit image function. In *Proceedings of the IEEE/CVF conference on computer vision and pattern recognition*, pp. 8628–8638, 2021.

Felipe Curcio, Pedro Castro, Augusto Fonseca, Rafaela Castro, Raquel Franco, Eduardo Ogasawara, Victor Stepanenko, Fabio Porto, Mariza Ferro, and Eduardo Bezerra. Towards a spatiotemporal fusion approach to precipitation nowcasting. *arXiv preprint arXiv:2505.19258*, 2025.

Zhangyang Gao, Cheng Tan, Lirong Wu, and Stan Z Li. Simvp: Simpler yet better video prediction. In *Proceedings of the IEEE/CVF conference on computer vision and pattern recognition*, pp. 3170–3180, 2022a.

Zhihan Gao, Xingjian Shi, Hao Wang, Yi Zhu, Yuyang Bernie Wang, Mu Li, and Dit-Yan Yeung. Earthformer: Exploring space-time transformers for earth system forecasting. *Advances in Neural Information Processing Systems*, 35:25390–25403, 2022b.

Zhihan Gao, Xingjian Shi, Boran Han, Hao Wang, Xiaoyong Jin, Danielle Maddix, Yi Zhu, Mu Li, and Yuyang Bernie Wang. Prediff: Precipitation nowcasting with latent diffusion models. *Advances in Neural Information Processing Systems*, 36:78621–78656, 2023.

Junchao Gong, Lei Bai, Peng Ye, Wanghan Xu, Na Liu, Jianhua Dai, Xiaokang Yang, and Wanli Ouyang. Cascast: Skillful high-resolution precipitation nowcasting via cascaded modelling. *arXiv preprint arXiv:2402.04290*, 2024a.

Junchao Gong, Siwei Tu, Weidong Yang, Ben Fei, Kun Chen, Wenlong Zhang, Xiaokang Yang, Wanli Ouyang, and Lei Bai. Postcast: Generalizable postprocessing for precipitation nowcasting via unsupervised blurriness modeling. *arXiv preprint arXiv:2410.05805*, 2024b.

Antoine Guédon and Vincent Lepetit. Sugar: Surface-aligned gaussian splatting for efficient 3d mesh reconstruction and high-quality mesh rendering. In *Proceedings of the IEEE/CVF Conference on Computer Vision and Pattern Recognition*, pp. 5354–5363, 2024.

Jintong Hu, Bin Xia, Bin Chen, Wenming Yang, and Lei Zhang. Gaussiansr: High fidelity 2d gaussian splatting for arbitrary-scale image super-resolution. In *Proceedings of the AAAI Conference on Artificial Intelligence*, volume 39, pp. 3554–3562, 2025.

Binbin Huang, Zehao Yu, Anpei Chen, Andreas Geiger, and Shenghua Gao. 2d gaussian splatting for geometrically accurate radiance fields. In *ACM SIGGRAPH 2024 conference papers*, pp. 1–11, 2024.

George J Huffman, David T Bolvin, Dan Braithwaite, Kuolin Hsu, Robert Joyce, Pingping Xie, and Soo-Hyun Yoo. Nasa global precipitation measurement (gpm) integrated multi-satellite retrievals for gpm (imerg). *Algorithm theoretical basis document (ATBD) version*, 4(26):30, 2015.

Bernhard Kerbl, Georgios Kopanas, Thomas Leimkühler, and George Drettakis. 3d gaussian splatting for real-time radiance field rendering. *ACM Trans. Graph.*, 42(4):139–1, 2023.

Dmitrii Kochkov, Janni Yuval, Ian Langmore, Peter Norgaard, Jamie Smith, Griffin Mooers, Milan Klöwer, James Lottes, Stephan Rasp, Peter Düben, et al. Neural general circulation models for weather and climate. *Nature*, 632(8027):1060–1066, 2024.

Remi Lam, Alvaro Sanchez-Gonzalez, Matthew Willson, Peter Wirnsberger, Meire Fortunato, Ferran Alet, Suman Ravuri, Timo Ewalds, Zach Eaton-Rosen, Weihua Hu, et al. Learning skillful medium-range global weather forecasting. *Science*, 382(6677):1416–1421, 2023.

Jaewon Lee and Kyong Hwan Jin. Local texture estimator for implicit representation function. In *Proceedings of the IEEE/CVF conference on computer vision and pattern recognition*, pp. 1929–1938, 2022.

Bo Li, Kaitao Xue, Bin Liu, and Yu-Kun Lai. Bbdm: Image-to-image translation with brownian bridge diffusion models. In *Proceedings of the IEEE/CVF conference on computer vision and pattern Recognition*, pp. 1952–1961, 2023.

Cheng-Chin Liu, Kathryn Hsu, Melinda S Peng, Der-Song Chen, Pao-Liang Chang, Ling-Feng Hsiao, Chin-Tzu Fong, Jing-Shan Hong, Chia-Ping Cheng, Kuo-Chen Lu, et al. Evaluation of five global ai models for predicting weather in eastern asia and western pacific. *npj Climate and Atmospheric Science*, 7(1):221, 2024.

Matthew P Lucas, Ryan J Longman, Thomas W Giambelluca, Abby G Frazier, Jared Mclean, Sean B Cleveland, Yu-Fen Huang, and Jonghyun Lee. Optimizing automated kriging to improve spatial interpolation of monthly rainfall over complex terrain. *Journal of Hydrometeorology*, 23(4): 561–572, 2022.

Ricardo Martin-Brualla, Noha Radwan, Mehdi SM Sajjadi, Jonathan T Barron, Alexey Dosovitskiy, and Daniel Duckworth. Nerf in the wild: Neural radiance fields for unconstrained photo collections. In *Proceedings of the IEEE/CVF conference on computer vision and pattern recognition*, pp. 7210–7219, 2021.

Tomoaki Mega, Tomoo Ushio, Matsuda Takahiro, Takuji Kubota, Misako Kachi, and Riko Oki. Gauge-adjusted global satellite mapping of precipitation. *IEEE Transactions on Geoscience and Remote Sensing*, 57(4):1928–1935, 2018.

Ben Mildenhall, Pratul P Srinivasan, Matthew Tancik, Jonathan T Barron, Ravi Ramamoorthi, and Ren Ng. Nerf: Representing scenes as neural radiance fields for view synthesis. *Communications of the ACM*, 65(1):99–106, 2021.

Thomas Müller, Alex Evans, Christoph Schied, and Alexander Keller. Instant neural graphics primitives with a multiresolution hash encoding. *ACM transactions on graphics (TOG)*, 41(4): 1–15, 2022.

Tung Nguyen, Johannes Brandstetter, Ashish Kapoor, Jayesh K Gupta, and Aditya Grover. Climax: A foundation model for weather and climate. *arXiv preprint arXiv:2301.10343*, 2023.

Wendell A Nuss and David W Titley. Use of multiquadric interpolation for meteorological objective analysis. AMS, 1994.

Young-Jae Park, Doyi Kim, Minseok Seo, Hae-Gon Jeon, and Yeji Choi. Data-driven precipitation nowcasting using satellite imagery. In *Proceedings of the AAAI Conference on Artificial Intelligence*, volume 39, pp. 28284–28292, 2025.

Jaideep Pathak, Shashank Subramanian, Peter Harrington, Sanjeev Raja, Ashesh Chattopadhyay, Morteza Mardani, Thorsten Kurth, David Hall, Zongyi Li, Kamyar Azizzadenesheli, et al. Fourcastnet: A global data-driven high-resolution weather model using adaptive fourier neural operators. *arXiv preprint arXiv:2202.11214*, 2022.

Long Peng, Anran Wu, Wenbo Li, Peizhe Xia, Xueyuan Dai, Xinjie Zhang, Xin Di, Haoze Sun, Renjing Pei, Yang Wang, et al. Pixel to gaussian: Ultra-fast continuous super-resolution with 2d gaussian modeling. *arXiv preprint arXiv:2503.06617*, 2025.

Ilan Price, Alvaro Sanchez-Gonzalez, Ferran Alet, Tom R Andersson, Andrew El-Kadi, Dominic Masters, Timo Ewalds, Jacklynn Stott, Shakir Mohamed, Peter Battaglia, et al. Probabilistic weather forecasting with machine learning. *Nature*, 637(8044):84–90, 2025.

Seppo Pulkkinen, Daniele Nerini, Andrés A Pérez Hortal, Carlos Velasco-Forero, Alan Seed, Urs Germann, and Loris Foresti. Pysteps: An open-source python library for probabilistic precipitation nowcasting (v1. 0). *Geoscientific Model Development*, 12(10):4185–4219, 2019.

Suman Ravuri, Karel Lenc, Matthew Willson, Dmitry Kangin, Remi Lam, Piotr Mirowski, Megan Fitzsimons, Maria Athanassiadou, Sheleem Kashem, Sam Madge, et al. Skilful precipitation nowcasting using deep generative models of radar. *Nature*, 597(7878):672–677, 2021.

Nigel M Roberts and Humphrey W Lean. Scale-selective verification of rainfall accumulations from high-resolution forecasts of convective events. *Monthly Weather Review*, 136(1):78–97, 2008.

Fengxue Ruan, Fengrui Chen, Qiao Liu, and Zhaobo Song. Fusion of satellite and gauge precipitation observations through coupling spatio-temporal properties with tree-based machine learning. *Journal of Hydrology*, pp. 134240, 2025.

Xingjian Shi, Zhourong Chen, Hao Wang, Dit-Yan Yeung, Wai-Kin Wong, and Wang-chun Woo. Convolutional lstm network: A machine learning approach for precipitation nowcasting. *Advances in neural information processing systems*, 28, 2015.

Vincent Sitzmann, Julien Martel, Alexander Bergman, David Lindell, and Gordon Wetzstein. Implicit neural representations with periodic activation functions. *Advances in neural information processing systems*, 33:7462–7473, 2020.

Casper Kaae Sønderby, Lasse Espeholt, Jonathan Heek, Mostafa Dehghani, Avital Oliver, Tim Salimans, Shreya Agrawal, Jason Hickey, and Nal Kalchbrenner. Metnet: A neural weather model for precipitation forecasting. *arXiv preprint arXiv:2003.12140*, 2020.

Mark Veillette, Siddharth Samsi, and Chris Mattioli. Sevir: A storm event imagery dataset for deep learning applications in radar and satellite meteorology. *Advances in Neural Information Processing Systems*, 33:22009–22019, 2020.

Petar Velickovic, Guillem Cucurull, Arantxa Casanova, Adriana Romero, Pietro Lio, Yoshua Bengio, et al. Graph attention networks. *stat*, 1050(20):10–48550, 2017.

Ting-Chun Wang, Ming-Yu Liu, Jun-Yan Zhu, Andrew Tao, Jan Kautz, and Bryan Catanzaro. High-resolution image synthesis and semantic manipulation with conditional gans. In *Proceedings of the IEEE conference on computer vision and pattern recognition*, pp. 8798–8807, 2018.

Guanjun Wu, Taoran Yi, Jiemin Fang, Lingxi Xie, Xiaopeng Zhang, Wei Wei, Wenyu Liu, Qi Tian, and Xinggang Wang. 4d gaussian splatting for real-time dynamic scene rendering. In *Proceedings of the IEEE/CVF conference on computer vision and pattern recognition*, pp. 20310–20320, 2024.

Yi Xiao, Lei Bai, Wei Xue, Kang Chen, Tao Han, and Wanli Ouyang. Fengwu-4dvar: Coupling the data-driven weather forecasting model with 4d variational assimilation. *arXiv preprint arXiv:2312.12455*, 2023.

Wanghan Xu, Fenghua Ling, Tao Han, Hao Chen, Wanli Ouyang, and LEI BAI. Generalizing weather forecast to fine-grained temporal scales via physics-ai hybrid modeling. *Advances in Neural Information Processing Systems*, 37:23325–23351, 2024.

Jingyu Yang, Sheng Shen, Huanjing Yue, and Kun Li. Implicit transformer network for screen content image continuous super-resolution. *Advances in Neural Information Processing Systems*, 34:13304–13315, 2021.

Ziyi Yang, Xinyu Gao, Wen Zhou, Shaohui Jiao, Yuqing Zhang, and Xiaogang Jin. Deformable 3d gaussians for high-fidelity monocular dynamic scene reconstruction. In *Proceedings of the IEEE/CVF conference on computer vision and pattern recognition*, pp. 20331–20341, 2024.

Donggeun Yoon, Minseok Seo, Doyi Kim, Yeji Choi, and Donghyeon Cho. Deterministic guidance diffusion model for probabilistic weather forecasting. *arXiv preprint arXiv:2312.02819*, 2023.

Demin Yu, Xutao Li, Yunming Ye, Baoquan Zhang, Chuyao Luo, Kuai Dai, Rui Wang, and Xunlai Chen. Diffcast: A unified framework via residual diffusion for precipitation nowcasting. In *Proceedings of the IEEE/CVF Conference on Computer Vision and Pattern Recognition*, pp. 27758–27767, 2024a.

Zehao Yu, Anpei Chen, Binbin Huang, Torsten Sattler, and Andreas Geiger. Mip-splatting: Alias-free 3d gaussian splatting. In *Proceedings of the IEEE/CVF conference on computer vision and pattern recognition*, pp. 19447–19456, 2024b.

Richard Zhang, Phillip Isola, Alexei A Efros, Eli Shechtman, and Oliver Wang. The unreasonable effectiveness of deep features as a perceptual metric. In *Proceedings of the IEEE conference on computer vision and pattern recognition*, pp. 586–595, 2018.

Xinjie Zhang, Xingtong Ge, Tongda Xu, Dailan He, Yan Wang, Hongwei Qin, Guo Lu, Jing Geng, and Jun Zhang. Gaussianimage: 1000 fps image representation and compression by 2d gaussian splatting. In *European Conference on Computer Vision*, pp. 327–345. Springer, 2024.

Yunxiang Zhang, Bingxuan Li, Alexandr Kuznetsov, Akshay Jindal, Stavros Diolatzis, Kenneth Chen, Anton Sochenov, Anton Kaplanyan, and Qi Sun. Image-gs: Content-adaptive image representation via 2d gaussians. In *Proceedings of the Special Interest Group on Computer Graphics and Interactive Techniques Conference Conference Papers*, pp. 1–11, 2025.

Lingting Zhu, Guying Lin, Jinnan Chen, Xinjie Zhang, Zhenchao Jin, Zhao Wang, and Lequan Yu. Large images are gaussians: High-quality large image representation with levels of 2d gaussian splatting. In *Proceedings of the AAAI Conference on Artificial Intelligence*, volume 39, pp. 10977–10985, 2025.

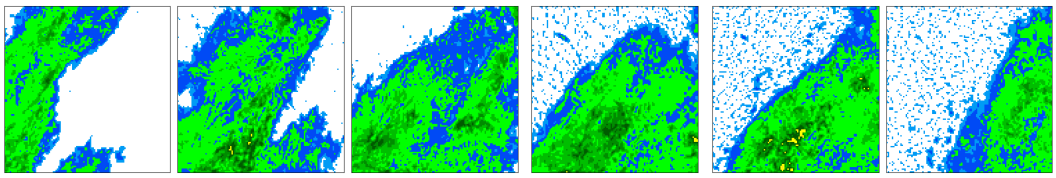

Figure 5: Examples of consecutive one-hour QCGS-generated frames. The last three frames exhibit rainfall patterns that were absent in the first three, indicating temporal inconsistencies. Such frame-to-frame mismatch can hinder the performance of video prediction models that rely on coherent temporal dynamics.

A Appendix

A.1 Inference data for precipitation forecasting

We further evaluated the utility of QCGS-generated radar fields as inference inputs for data-driven precipitation forecasting models. Specifically, we tested three representative baselines: MetNet-v2 (Sønderby et al., 2020), PreDiff (Gao et al., 2023), and SimVP (Gao et al., 2022a). We followed a standard nowcasting protocol in which seven past frames at ten-minute intervals are used as input and six future frames (up to +60 minutes) are predicted. MetNet-v2 directly predicts precipitation at the target lead time, while PreDiff and SimVP follow a many-to-many forecasting scheme.

All baselines were originally trained only in the radar to radar setting, and we performed no retraining or adaptation when using QCGS inputs. Despite this clear train to test mismatch, QCGS-driven forecasting still preserved meaningful predictive skill. As summarized in Table 3, the CSI at the 1 mm threshold decreased from 0.664 to 0.381 for PreDiff and from 0.591 to 0.252 for SimVP. MetNet-v2 showed only a small decrease, from 0.390 to 0.374.

We attribute this degradation to two main factors. First, QCGS does not currently enforce temporal coherence across frames, and this results in inconsistencies in the time dimension (see Fig. 5). Second, QCGS produces fields that are closer to AWS gauge values, while radar reflectivity is empirically calibrated to rain rate through the standard Z-R relationship. This creates a mismatch for forecasting models that were trained only with radar inputs.

The smaller degradation observed in MetNet-v2 is consistent with its single-step prediction design, which is less sensitive to inter-frame consistency than many-to-many models.

Future work includes extending QCGS with temporal conditioning to provide coherent dynamics across consecutive frames, and retraining downstream forecasting models directly on QCGS-generated inputs. This may reduce the performance gap between QCGS-based and radar-based forecasting.

Table 3: Forecasting performance at +60 minutes using QCGS-generated radar fields as inputs. Baselines were trained only on radar-to-radar data and used without retraining.

Model	**CSI@1mm (R→R)**	**CSI@1mm (QCGS→R)**
MetNet-v2 Sønderby et al. (2020)	0.390	0.374
SimVP Gao et al. (2022a)	0.591	0.252
PreDiff Gao et al. (2023)	0.664	0.381

A.2 QCGS vs. Radar

Before comparing QCGS with radar products, Figure 8 provides an overview of the qualitative differences among AWS observations, global rainfall products, and QCGS. As shown, QCGS better preserves fine-scale precipitation structures while mitigating large-scale biases commonly observed

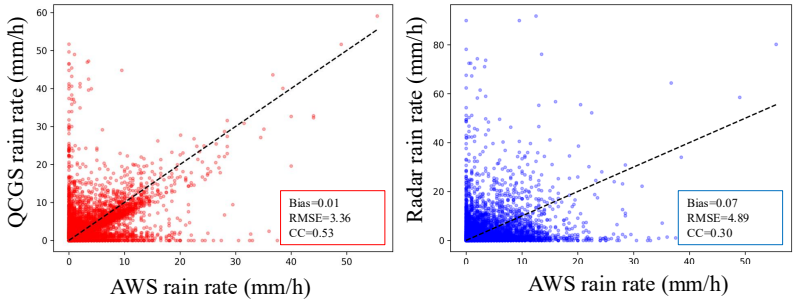

Figure 6: Bias, RMSE, and correlation coefficient (CC) of AWS rain rate compared with QCGS and radar. QCGS consistently achieves lower bias and RMSE and higher CC relative to radar, demonstrating closer agreement with gauge observations.

in conventional global products. This contextual comparison highlights the importance of evaluating QCGS against radar-derived fields.

Radar rainfall products are derived by converting reflectivity (Z) into rain rate (R) through empirical Z–R relations. As such, they are not direct rainfall measurements and often suffer from systematic biases, especially in convective storms or orographically complex regions. In contrast, QCGS is trained on radar targets but incorporates AWS anchors at inference. Remarkably, the resulting fields often align more closely with gauge observations than radar itself. This suggests that QCGS not only reproduces radar-like spatial patterns but also implicitly corrects radar biases by leveraging point-level AWS data.

Figure 6 provides quantitative evidence: compared to radar, QCGS achieves lower bias and RMSE and higher correlation coefficients when evaluated against AWS observations. These improvements indicate that the inclusion of AWS anchors yields rainfall fields that are both more accurate and more consistent with ground truth.

Figure 7 presents case studies where gridded fields are directly matched with AWS locations. Here, QCGS preserves rainfall intensity more faithfully than radar, particularly in high-rainfall events. Importantly, AWS evaluations were performed using standard point-to-grid matching with spatial averaging, ensuring that the observed improvements are not an artifact of directly injecting AWS values but reflect genuine gains in field representation.

Taken together, these findings highlight a potential paradigm shift: QCGS offers rainfall maps that are simultaneously radar-consistent and gauge-calibrated, bridging the gap between remote sensing products and in-situ truth. In the long term, this property points to the possibility of QCGS serving as a complementary or even superior alternative to radar-derived rainfall estimates.

A.3 Additional quantitative analysis.

Beyond continuous metrics such as RMSE and correlation, it is important to evaluate precipitation skill in a categorical manner across different rainfall intensities. To provide a more complete assessment, we present two complementary threshold-based analyses.

Table 4 reports CSI scores at 1, 5, and 10 mm using hourly data. These thresholds reflect light, moderate, and heavy rainfall. QCGS consistently outperforms satellite products across all intensity levels, and the improvement is most pronounced for heavy rainfall, where accurate detection is crucial.

To complement the hourly evaluation, Table 5 presents daily POD, FAR, and CSI metrics at 10, 50, and 100 mm per day. This daily-scale analysis captures the model's ability to detect accumulated precipitation extremes, which are critical for hydrological and disaster-related applications. QCGS

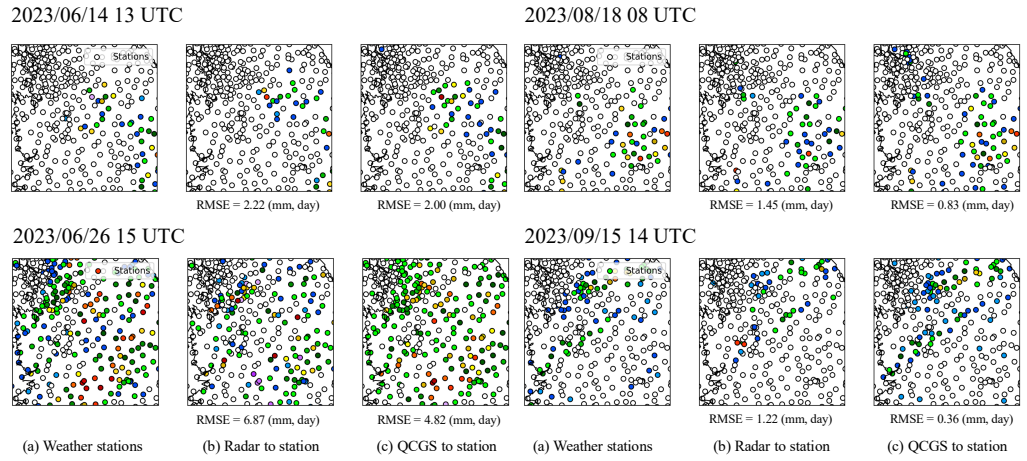

Figure 7: Case studies comparing QCGS and radar against AWS stations. Gridded fields are spatially matched to AWS locations, showing that QCGS preserves local rainfall intensities more faithfully than radar.

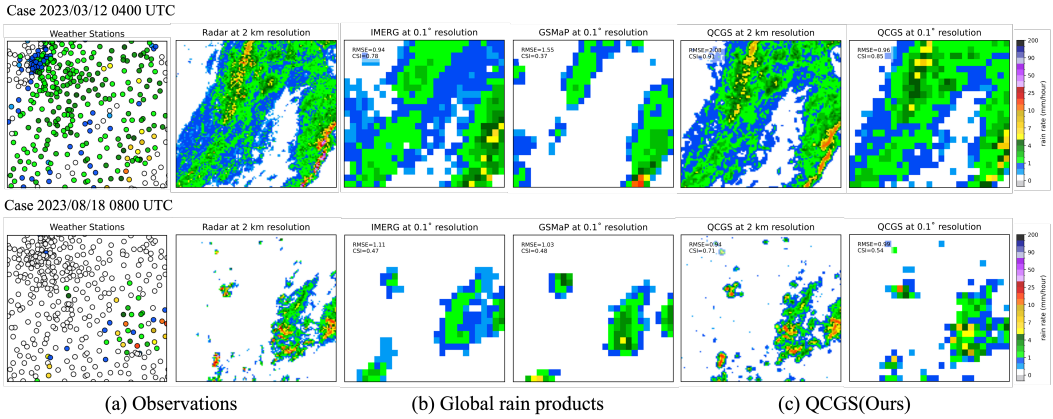

Figure 8: Qualitative comparison of observations, global rainfall products, and QCGS. QCGS preserves fine-scale precipitation structures and reduces large-scale biases relative to conventional products.

achieves the best POD and CSI across all daily thresholds, while maintaining reasonable FAR values. In contrast, satellite products either miss many high-rainfall days or exhibit high false-alarm rates.

Together, the hourly and daily analyses provide a comprehensive characterization of model performance. QCGS consistently surpasses satellite products across all intensity levels and temporal scales, confirming its ability to reconstruct precipitation structure more faithfully than existing methods.

A.4 Cross-domain Experimental Results

As shown in Fig. 9, we use Regions 1 and 2 (top) for training, while Regions 3 and 4 (bottom) are excluded from training. Table 6 presents the experimental results. QCGS shows only a small performance drop in unseen regions. We believe this is due to two reasons: (1) although the regions differ, they are geographically close and share similar meteorological patterns, and (2) the number of activated AWS stations varies significantly depending on the rainfall intensity. For example, heavy-rain days may activate more than 700 AWS stations, while light-rain days may activate fewer than 100. This naturally exposes the model to diverse spatial AWS configurations during training.

Table 4: CSI scores at different rainfall thresholds (mm per hour) using hourly data. QCGS is evaluated at multiple spatial resolutions (0.5, 2, and 10 km).

Threshold	QCGS (0.5 km)	QCGS (2 km)	QCGS (10 km)	IMERG	GSMaP
1	0.657	0.703	0.506	0.366	0.308
5	0.415	0.483	0.306	0.140	0.129
10	0.311	0.401	0.232	0.046	0.065

Table 5: Categorical POD, FAR, and CSI scores at different rainfall thresholds (mm per day) for daily accumulation data.

	POD			FAR			CSI		
Threshold	10	50	100	10	50	100	10	50	100
QCGS	**0.703**	**0.579**	**0.646**	**0.125**	**0.329**	**0.423**	**0.657**	**0.455**	**0.434**
IMERG	0.679	0.369	0.117	0.267	0.616	0.614	0.541	0.173	0.039
GSMaP	0.591	0.358	0.277	0.262	0.710	0.754	0.493	0.165	0.119
MSWEP	0.714	0.315	0.096	0.286	0.554	0.584	0.553	0.191	0.067

A.5 Visual Quality Ablation Study

Figure 10 presents a qualitative comparison among Radar, QCGS, AWS-only, and Satellite-only baselines. The AWS-only reconstruction exhibits isolated Gaussian blobs, which occur because point-based gauge measurements cannot fully represent the entire spatial domain. The Satellite-only baseline appears noticeably blurred, largely due to relying solely on pixel-wise MSE loss without ground-level anchors. In contrast, QCGS produces sharper, more coherent precipitation structures that closely resemble radar observations, benefiting from its Gaussian splatting–based rendering and AWS–satellite fusion. These visual results further confirm that QCGS delivers superior perceptual fidelity compared to other ablated variants.

A.6 Visual Quality Comparison with Classical Interpolation

Figure 11 presents a qualitative comparison between classical interpolation methods and the AWS-only variant of QCGS. All methods are evaluated under identical input, target, and output conditions to ensure a fair comparison. As shown in the figure, QCGS produces noticeably sharper and more coherent precipitation structures compared to classical approaches, demonstrating superior visual quality.

A.7 Additional qualitative analysis.

This section reports qualitative examples, which are randomly sampled rather than cherry-picked, to ensure fair illustration of model behavior.

Figure 8 highlights a representative case. Radar reports an area of intense rainfall, whereas QCGS produces a similar spatial pattern but with lower intensity. At first glance, this could be interpreted as an underestimation by QCGS. However, inspection of AWS gauge measurements (case: 2023/03/12 04:00) reveals that strong rainfall was not observed at ground level. This indicates that in this instance, radar likely overestimated rainfall intensity, while QCGS produced fields more consistent with in-situ truth. Such cases highlight the value of incorporating gauge anchors, which allow QCGS to mitigate biases inherent in radar-only products.

Figure 12 presents two challenging cases (2023/07/11 07 UTC and 2023/08/09 12 UTC) where QCGS underperforms compared to conventional products. In both events, QCGS struggles to capture the spatial extent and intensity of the observed precipitation system. This limitation is particularly evident in convective episodes with rapidly evolving structures, where sparse AWS anchors provide insufficient coverage. The examples illustrate that while QCGS often achieves strong performance, it is not universally superior across all conditions. These cases highlight the need for future extensions, such as incorporating temporal coherence or additional observation sources, to further improve robustness.

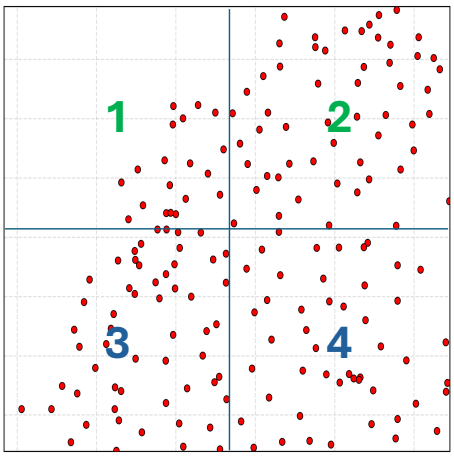

Figure 9: Training and evaluation regions. Regions 1 and 2 are used for model training, while Regions 3 and 4 are excluded.

Metric	Cross-domain	In-domain
RMSE↓	1.01	1.00
CSI↑	0.76	0.76
Bias=1	1.03	1.03
FSS=1 (ne=5)	0.96	0.96
LPIPS↓	0.25	0.19
pCC↑	0.93	0.93
rCC↑	0.91	0.92

Table 6: Cross-domain evaluation results.

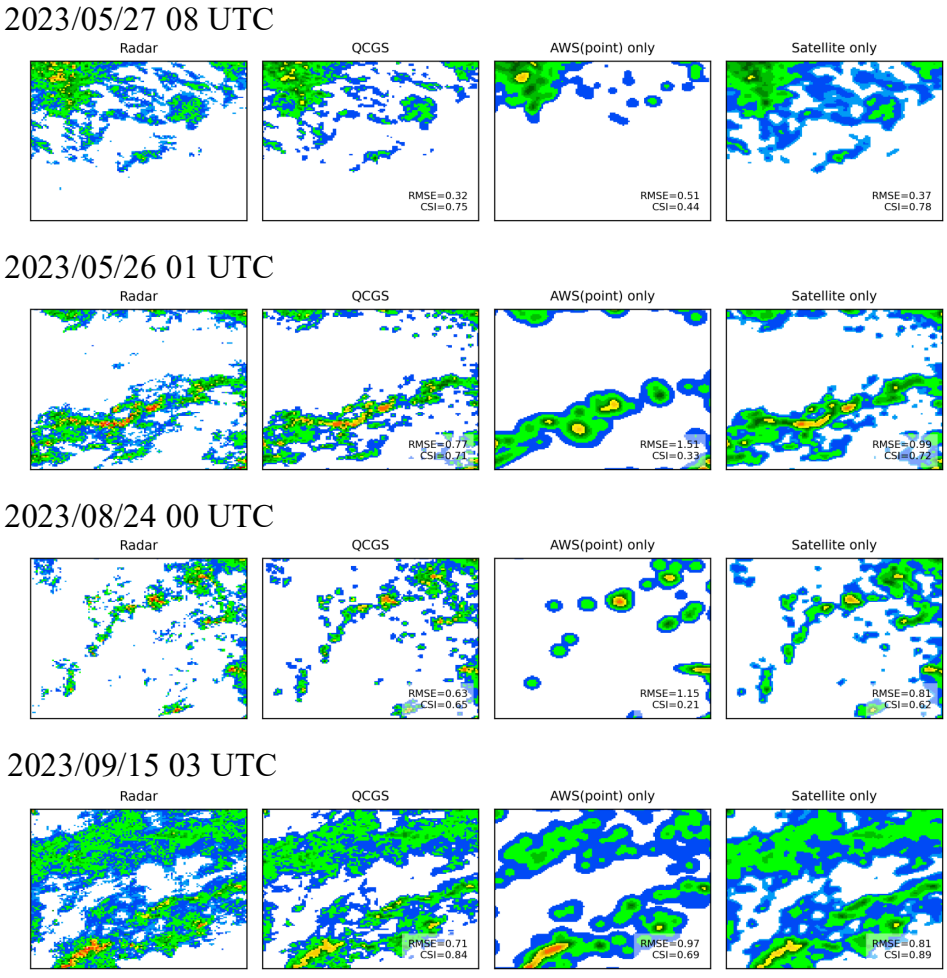

Figure 10: Visual comparison of Radar, QCGS, AWS-only, and Satellite-only across several cases.

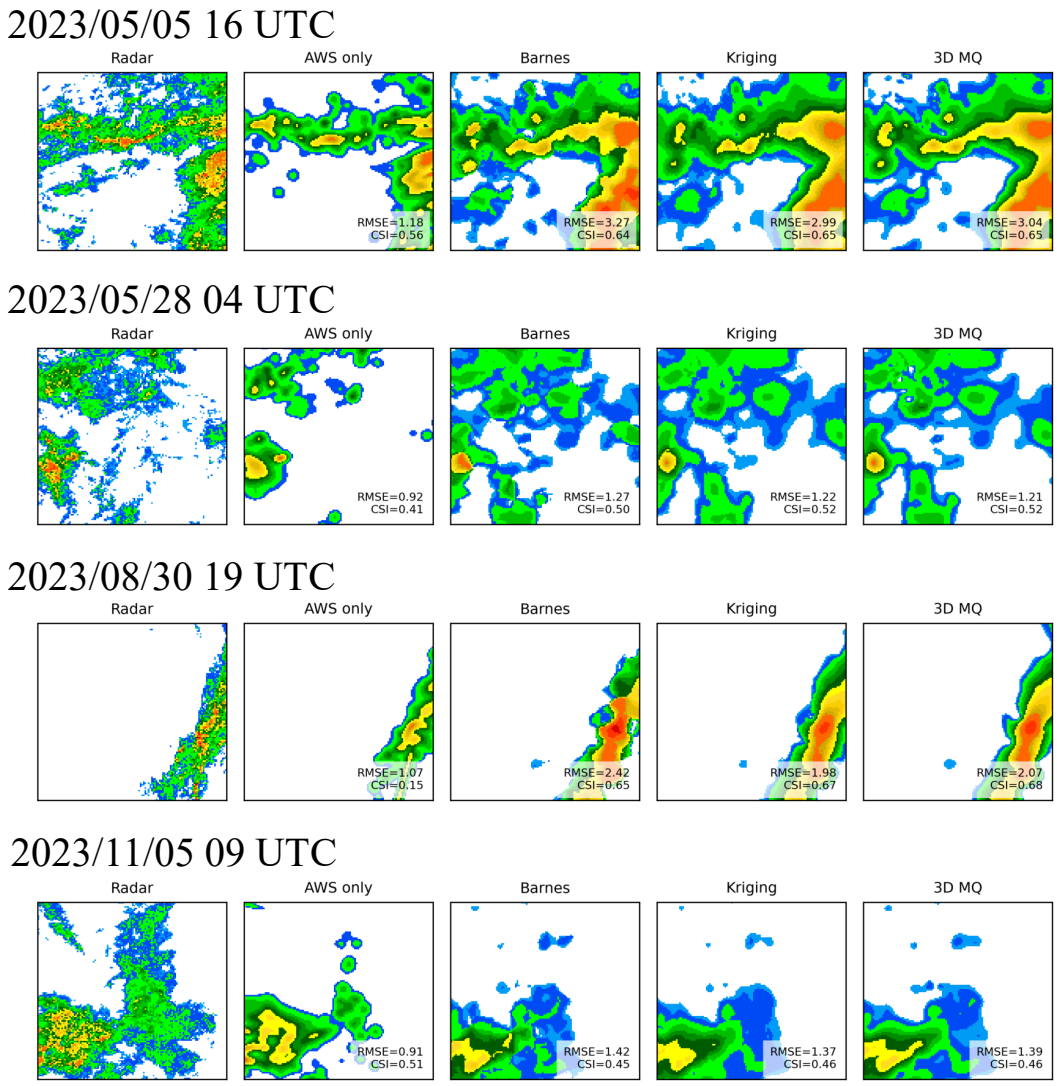

Figure 11: Qualitative comparison between classical interpolation methods and QCGS (AWS-only).

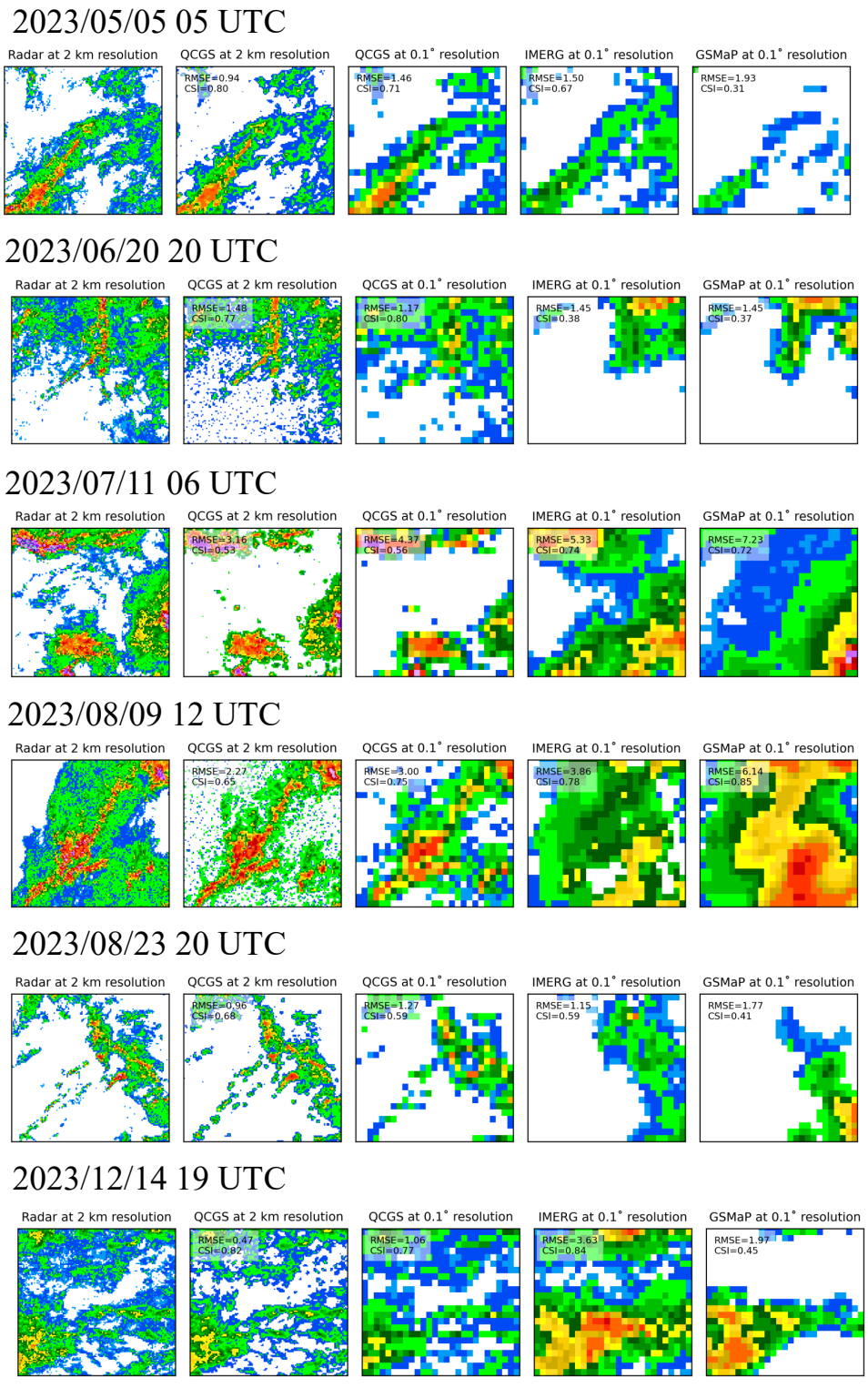

Figure 12: Qualitative comparison of precipitation fields from radar, QCGS, IMERG, and GSMaP. Radar provides the reference, while QCGS preserves fine-scale structures more faithfully than global products. IMERG and GSMaP show smoother fields with biases in convective regions.

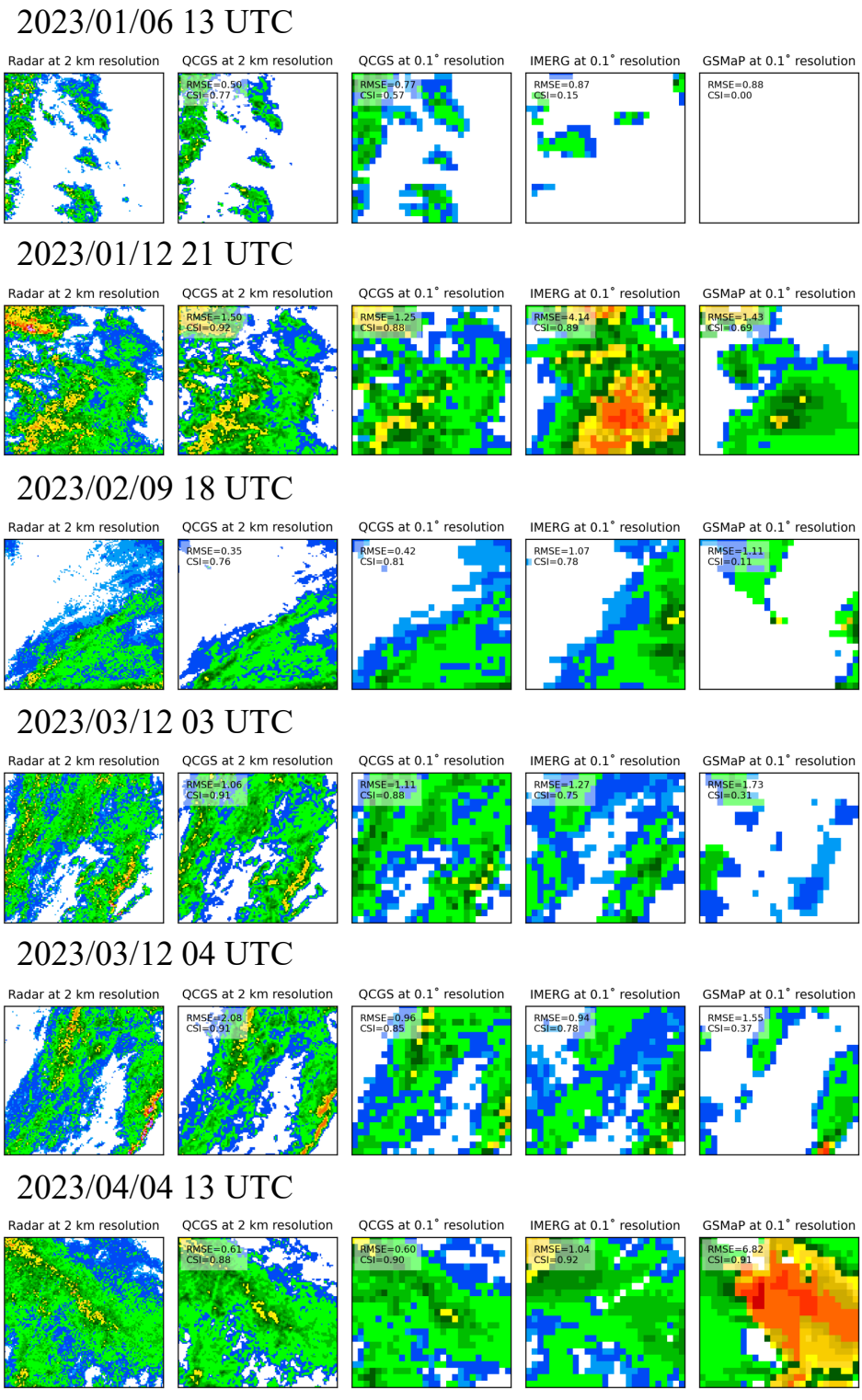

Figure 13: Qualitative comparison of precipitation fields from radar, QCGS, IMERG, and GSMaP. Radar provides the reference, while QCGS preserves fine-scale structures more faithfully than global products. IMERG and GSMaP show smoother fields with biases in convective regions.